Hyperthermal reactions of O(p3sP) with hydrogen and methane
by Donna Joan Garton

A dissertation submitted in partial fulfillment of the requirements for the degree of Doctor of Philosophy in Chemistry
Montana State University

Abstract:
Hyperthermal reactions of O(3P) occur at the surfaces and in the exhaust gases of spacecraft that travel through the residual atmosphere of the Earth at high altitudes (200-600 km). These reactions may degrade materials through oxidation and erosion, or they may yield internally excited reaction products which emit radiation and contribute to the "signature" of a rocket plume. Crossed-beams experiments were used to study model reactions of O(3P) with H2, D2, CH4, and CD4 at center-of-mass collision energies in the range 8-75 kcal mol^-1. Interpretation of the experimental results has been strengthened by theoretical calculations carried out by collaborators. A study of the OH scattered flux as a function of collision energy has led to the determination of an experimental excitation function in the threshold region for the O(3P)+H2 → OH+H reaction. The experimental excitation function clearly matched the theoretical prediction, which confirmed that the laser-detonation source produces O(3P) atoms. The excitation function for the O(3P) + H2 reaction and the dynamics of the O(3P) + D2 reaction, observed experimentally for the first time, demonstrate that these reactions proceed mainly on triplet potential energy surfaces, with little or no intersystem crossing. Experiments on the reactions of O(3P) with methane have revealed a previously unobserved reaction pathway, which involves H-atom elimination: O(3P) + CH4 → OCH3 + H. The excitation function for this reaction has been measured, and the reaction barrier has been determined to be □46 kcal mol^-1. In addition, the expected H-atom abstraction reaction, O(3P) + CH4 → CH3 + OH, has been observed, and the dynamics have been investigated. Theoretical calculations identify a triplet-singlet curve crossing below the triplet barrier for the H-atom elimination reaction, but the observed dynamics indicate reaction exclusively on the two lowest-lying triplet surfaces. While it remains to be seen whether intersystem crossing will affect the outcome of other reactions involving hyperthermal atomic oxygen, unknown reactions which have high barriers are likely to be common in extreme environments such as low-Earth orbit, where spacecraft surfaces and exhaust gases suffer high-energy collisions with ambient atomic oxygen.

HYPERTHERMAL REACTIONS OF O(^3P) WITH HYDROGEN AND METHANE

by

Donna Joan Garton

A dissertation submitted in partial fulfillment
of the requirements for the degree

of

Doctor of Philosophy

in

Chemistry

MONTANA STATE UNIVERSITY
Bozeman, Montana

April 2004

APPROVAL

of a dissertation submitted by

Donna Joan Garton

This dissertation has been read by each member of the dissertation committee and has been found to be satisfactory regarding content, English usage, format, citations, bibliographic style, and consistency, and is ready for submission to the College of Graduate Studies.

Lee Spangler _____ 4/16/04
Date

Approved for the Department of Chemistry

Paul A. Grieco _____ 4-16-04
Date

Approved for the College of Graduate Studies

Bruce McLeod _____ 4-19-04
Date

STATEMENT OF PERMISSION TO USE

In presenting this dissertation in partial fulfillment of the requirements for a doctoral degree at Montana State University, I agree that the Library shall make it available to borrowers under rules of the Library. I further agree that copying of this dissertation is allowable only for scholarly purposes, consistent with "fair use" as prescribed in the U.S. Copyright Law. Requests for extensive copying or reproduction of this dissertation should be referred to Bell & Howell Information and Learning, 300 North Zeeb Road, Ann Arbor, Michigan 48106, to whom I have granted "the exclusive right to reproduce and distribute my dissertation in and from microform along with the non-exclusive right to reproduce and distribute my abstract in any format in whole or in part."

Signature 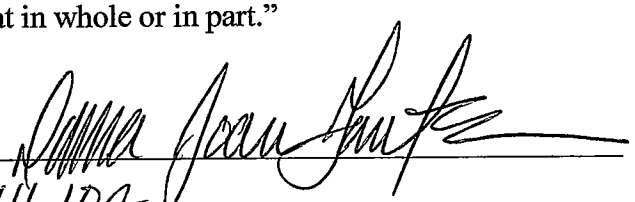

Date 4/16/04

TABLE OF CONTENTS

LIST OF FIGURES vi

ABSTRACT xi

1. INTRODUCTION 1

Spacecraft in the Low-Earth Orbital Environment 1
Polymer Erosion in LEO 2
Chemiluminescence From O-Atom Reactions with Rocket Plumes 3
From LEO to the Laboratory:
Simulating Oxygen Atom Reactions Occurring in LEO 4
Relevant Oxygen Atom Chemistry 5
Oxygen Atom Reactions with Hydrogen 5
Oxygen Atom Reactions with Alkanes 6
Initial Reactions of $O(^3P)$ with a Hydrocarbon Surface 7
Experiment-Theory Coupling 8
References 10

2. METHODS 14

Crossed Molecular Beams Experiments 14
Beam Sources 16
Laser Detonation Source of Hyperthermal Atomic Oxygen 16
Supersonic Beam of Hydrogen and Alkanes 18
Experiment Timing 20
Center-of-Mass to Laboratory Transformation 23
Experimental Resolution 26
References 30

3. EXCITATION FUNCTION FOR THE $O(^3P) + H_2 \rightarrow OH + H$ REACTION: CHARACTERIZATION OF THE OXYGEN ATOM ELECTRONIC STATE IN THE HYPERTHERMAL BEAM 31

Introduction 31
Experimental Details 33
Results and Analysis 35
Discussion 35
Conclusion 40
References 41

TABLE OF CONTENTS - CONTINUED

4. INELASTIC AND REACTIVE SCATTERING DYNAMICS OF $O(^3P) + D_2$ 43

Introduction 43
Experimental Details 47
Results and Analysis 48
Inelastic Scattering 49
Reactive Scattering 52
Discussion 57
Conclusion 63
References 64

5. EXCITATION FUNCTION FOR THE $O(^3P) + CH_4 \rightarrow OCH_3 + H$ REACTION 66

Introduction 66
Experimental Details 68
Results and Analysis 72
Discussion 75
Conclusion 80
References 82

6. INELASTIC AND REACTIVE SCATTERING DYNAMICS OF $O(^3P)$ COLLISIONS WITH CH_4 AND CD_4 84

Introduction 84
Experimental Details 89
Results and Analysis 90
$O(^3P) + CH_4$ 90
$O(^3P) + CD_4$ 94
Relative Yields of Primary Reactive Pathways for $O(^3P) + CH_4$ 107
Reactions Involving Molecular Oxygen 109
Discussion 111
Conclusion 118
References 120

7. CONCLUSION 121

LIST OF FIGURES

Figure Page

2.1. Schematic diagram of the crossed molecular beams apparatus at Montana State University. 15

2.2. Representative oxygen atom beam time-of-flight distributions. The overall beam distribution (dashed line) was narrowed in all of the experiments with the use of a synchronize chopper wheel. 20

2.3. Example timing diagram used in the experiments. 21

3.1. A Newton diagram for the OH + H channel of the $O(^3P) + H_2$ reaction at E_{coll} = 15 kcal mol^{-1}. 32

3.2. Oxygen-atom beam velocity distributions created from chopping the overall beam pulse with a velocity selector wheel rotating at 270 Hz. 34

3.3. Time-of-flight (TOF) distributions of inelastically scattered O (top) and reactively scattered OH (bottom), collected with a detector angle of 5° with respect to the oxygen-atom beam. 36

3.4. Predicted excitation curves (lines) for the $O + H_2$ reaction on singlet and triplet surfaces and experimental data points (circles) for the relative flux of scattered OH product. 37

3.5. Calculated excitation functions from Schatz *et al.* for the $O(^3P) + H_2 \rightarrow$ OH + H reaction. 39

4.1. A Newton diagram showing inelastically scattered O and reactively scattered OD from hyperthermal collisions of $O(^3P)$ with D_2 at E_{coll} = 25 kcal mol^{-1}. 44

4.2. Potential energy curves along the minimum energy path for the triplet reaction with H_2 at slightly bent O-H-H geometries. 46

4.3. Representative time-of-flight distributions of inelastically scattered O following collisions with D_2 at E_{coll} = 25 kcal mol^{-1}. 50

LIST OF FIGURES - CONTINUED

Figure Page

4.4. Laboratory angular distribution of $m/z = 16$ (O^+) inelastically scattered from D_2 with $E_{coll} = 25$ kcal mol^{-1}. 50

4.5. Center-of-mass translational energy distribution for the inelastic scattering of O from D_2 at $E_{coll} = 25$ kcal mol^{-1}, derived from the TOF and laboratory angular distributions for $m/z = 16$ (O^+) through the forward convolution method. 51

4.6. Center-of-mass angular distribution for O atoms that scatter inelastically from D_2 at $E_{coll} = 25$ kcal mol^{-1}, derived from the TOF and laboratory angular distributions for $m/z = 16$ (O^+) through the forward convolution method. 51

4.7. Center-of-mass velocity-flux map superimposed on a Newton diagram for O atoms that scatter inelastically from D_2 at $E_{coll} = 25$ kcal mol^{-1}. 53

4.8. Representative time-of-flight distributions of reactively scattered OD following reaction of $O(^3P)$ with D_2 at $E_{coll} = 25$ kcal mol^{-1}. 55

4.9. Laboratory angular distribution of the OD product from the reaction of $O(^3P)$ with D_2 at $E_{coll} = 25$ kcal mol^{-1}. 55

4.10. Center-of-mass translational energy distributions for the $O(^3P) + D_2 \rightarrow$ OD +D reaction at $E_{coll} = 25$ kcal mol^{-1}. 56

4.11. Center-of-mass angular distributions for the $O(^3P) + D_2 \rightarrow$ OD +D reaction at $E_{coll} = 25$ kcal mol^{-1}. 56

4.12. Center-of-mass velocity-flux map superimposed on a Newton diagram for the OD product from the reaction of $O(^3P) + D_2 \rightarrow$ OD + D at $E_{coll} = 25$ kcal mol^{-1}. 58

4.13. Center-of-mass velocity-flux map superimposed on a Newton diagram for the OD product from the reaction of $O(^3P) + D_2 \rightarrow$ OD + D at $E_{coll} = 25$ kcal mol^{-1}. 59

4.14. Center-of-mass velocity-flux map superimposed on a Newton diagram for the OD product from the reaction of $O(^3P) + D_2 \rightarrow$ OD + D at $E_{coll} = 25$ kcal mol^{-1}. 60

LIST OF FIGURES - CONTINUED

Figure Page

5.1. Energy diagram for the possible reaction channels in the reaction of $O(^3P)$ with CH_4. 67

5.2. A Newton diagram for the OCH_3 + H channel of the $O(^3P)$ + CH_4 reaction at E_{coll} = 62 kcal mol^{-1}. 69

5.3. Time-of-flight distributions collected at five different mass-to-charge ratios that indicate the formation of oxygen-containing products from the reaction of $O(^3P)$ with CH_4. 73

5.4. Time-of-flight (TOF) distributions of inelastically scattered O (top) and reactively scattered OCH_3 (bottom; detected at m/z=29), collected with the detector angle adjusted to coincide with the direction of the center-of-mass velocity vector, which ranged from 4 to 7° with respect to the oxygen-atom beam direction. 76

5.5. Experimental and calculated excitation functions (cross section vs. collision energy) for the $O(^3P) + CH_4 \rightarrow OCH_3 + H$ reaction. 77

5.6. Saddle point structures associated with the $O(^3P) + CH_4 \rightarrow OCH_3 + H$ reaction. 79

6.1. A Newton diagram for the for the reaction of $O(^3P)$ with CD_4 at E_{coll} = 78 kcal mol^{-1}. 87

6.2. A Newton diagram showing the OH + CH_3 and H + OCH_3 channels of the $O(^3P)$ + CH_4 reacton at E_{coll} = 67 kcal mol^{-1}. 88

6.3. Representative time-of-flight distributions of reactively scattered OH following reaction of $O(^3P)$ with CH_4 at E_{coll} = 67 kcal mol^{-1}. 91

6.4. Laboratory angular distribution of the OH product from the reaction of $O(^3P)$ with CH_4. 91

6.5. Center-of-mass translational energy distribution for the $O(^3P) + CH_4 \rightarrow$ OH + CH_3 reaction at E_{coll} = 67 kcal mol^{-1} derived from the TOF and laboratory angular distributions for m/z = 17 (OH^+) through the forward convolution method. 92

LIST OF FIGURES - CONTINUED

Figure Page

6.6. The solid line is the center-of-mass angular distribution of the OH product from the reaction of $O(^3P) + CH_4 \rightarrow OH + CH_3$ reaction at $E_{coll} = 67$ kcal mol^{-1}, derived from the TOF and laboratory angular distributions for $m/z = 17$ (OH^+) through the forward convolution method. 92

6.7. Center-of-mass velocity-flux map, superimposed on a Newton diagram, for the OH product from the reaction, $O(^3P) + CH_4 \rightarrow OH + CH_3$, at $E_{coll} = 67$ kcal mol^{-1}. 94

6.8. Representative time-of-flight distributions of inelastically scattered CD_4 following collisions with $O(^3P)$ at $E_{coll} = 76$ kcal mol^{-1}. 96

6.9. Laboratory angular distribution of CD_4 that scatters inelastically from $O(^3P)$ with $E_{coll} = 76$ kcal mol^{-1}. 96

6.10. Center-of-mass translational energy distribution for the inelastic scattering of CD_4 from $O(^3P)$ at $E_{coll} = 76$ kcal mol^{-1} derived from the TOF and laboratory angular distributions for $m/z = 20$ (CD_4^+) through the forward convolution method. 97

6.11. Center-of-mass angular distribution of CD_4 product from inelastic scattering from $O(^3P)$ at $E_{coll} = 76$ kcal mol^{-1} derived from the TOF and laboratory angular distributions for $m/z = 20$ (CD_4^+) through the forward convolution method. 97

6.12. Center-of-mass velocity-flux map superimposed on a Newton diagram for CD_4 inelastically scattering from $O(^3P)$ at $E_{coll} = 76$ kcal mol^{-1}. 99

6.13. Representative time-of-flight distributions collected at five different mass-to-charge ratios resulting from $O(^3P)$ colliding with CD_4 at $E_{coll} = 73$ kcal mol^{-1} and at $\Theta_{LAB} = 6.5°$. 100

6.14. Time-of-flight distributions of $m/z = 15$ (CH_3^+) collected at $E_{coll} =$ 67 kcal mol^{-1} in the reaction of $O(^3P)$ with CH_4 (above). Time-of-flight distributions of $m/z = 18$ (CD_3^+) collected at $E_{coll} = 76$ kcal mol^{-1} in the reaction of $O(^3P)$ with CD_4 (below). 101

LIST OF FIGURES - CONTINUED

Figure Page

6.15. Newton diagrams for $O(^3P) + CD_4 \rightarrow OCD_3 + D$, showing the OCD_3 Newton circle (blue). If the OCD_3 undergoes secondary dissociation to OCD_2, its scattering will appear as a second Newton circle (red) with its center-of-mass directly on and all around the OCD_3 Newton circle. 103

6.16. Representative time-of-flight distributions of the OCD_3 product from the reaction of $O(^3P) + CD_4 \rightarrow OCD_3 + D$ at $E_{coll} = 76$ kcal mol^{-1}. 105

6.17. Laboratory angular distribution of the OCD_3 product from the reaction of $O(^3P)$ with CD_4 with $E_{coll} = 76$ kcal mol^{-1}. 105

6.18. The solid line represents the center-of-mass translational energy distribution for the $O(^3P) + CD_4 \rightarrow D + CD_3O$ reaction at $E_{coll} = 78$ kcal mol^{-1}, obtained from the TOF and laboratory angular distributions for $m/z = 30$ (CDO^+) through the forward convolution method. 106

6.19. Center-of-mass angular distribution of the CD_3O product from the reaction of $O(^3P) + CD_4 \rightarrow D + CD_3O$ reaction at $E_{coll} = 78$ kcal mol^{-1}, obtained from the TOF and laboratory angular distributions for $m/z = 30$ (CDO^+) through the forward convolution method. 106

6.20. A Newton diagram for $O(^3P) + CD_4 \rightarrow OCD_3 + D$, showing the OCD_3 Newton circle (blue). If the OCD_3 undergoes secondary dissociation to OCD_2, its scattering will appear as a set of secondary Newton circles (red) with their center-of-masses directly on and all around the OCD_3 Newton circle. 116

ABSTRACT

Hyperthermal reactions of $O(^3P)$ occur at the surfaces and in the exhaust gases of spacecraft that travel through the residual atmosphere of the Earth at high altitudes (200-600 km). These reactions may degrade materials through oxidation and erosion, or they may yield internally excited reaction products which emit radiation and contribute to the "signature" of a rocket plume. Crossed-beams experiments were used to study model reactions of $O(^3P)$ with H_2, D_2, CH_4, and CD_4 at center-of-mass collision energies in the range 8 - 75 kcal mol^{-1}. Interpretation of the experimental results has been strengthened by theoretical calculations carried out by collaborators. A study of the OH scattered flux as a function of collision energy has led to the determination of an experimental excitation function in the threshold region for the $O(^3P) + H_2 \rightarrow OH + H$ reaction. The experimental excitation function clearly matched the theoretical prediction, which confirmed that the laser-detonation source produces $O(^3P)$ atoms. The excitation function for the $O(^3P) + H_2$ reaction and the dynamics of the $O(^3P) + D_2$ reaction, observed experimentally for the first time, demonstrate that these reactions proceed mainly on triplet potential energy surfaces, with little or no intersystem crossing. Experiments on the reactions of $O(^3P)$ with methane have revealed a previously unobserved reaction pathway, which involves H-atom elimination: $O(^3P) + CH_4 \rightarrow OCH_3 + H$. The excitation function for this reaction has been measured, and the reaction barrier has been determined to be ~46 kcal mol^{-1}. In addition, the expected H-atom abstraction reaction, $O(^3P) + CH_4 \rightarrow CH_3 + OH$, has been observed, and the dynamics have been investigated. Theoretical calculations identify a triplet-singlet curve crossing below the triplet barrier for the H-atom elimination reaction, but the observed dynamics indicate reaction exclusively on the two lowest-lying triplet surfaces. While it remains to be seen whether intersystem crossing will affect the outcome of other reactions involving hyperthermal atomic oxygen, unknown reactions which have high barriers are likely to be common in extreme environments such as low-Earth orbit, where spacecraft surfaces and exhaust gases suffer high-energy collisions with ambient atomic oxygen.

INTRODUCTION

Spacecraft in the Low-Earth Orbital Environment

The low-Earth orbital environment, having an altitude range of 200 to 600 km, is host to many short-term and long-term spacecraft, including the International Space Station (350-460 km), space shuttle (~300 km), a large number of private and government satellites, such as communications satellites, and missiles. During their time in low-Earth orbit (LEO) these spacecraft are surrounded by a strongly oxidizing residual atmosphere predominantly composed of atomic oxygen.[1] At typical space shuttle altitudes, the oxygen atom number density is on the order of 10^9 cm^{-3}.[1-3] Most of the oxygen atoms are in the ground, or $O(^3P)$, electronic state, while only 0.001 percent is estimated to be in the first excited state, $O(^1D)$.[2] In addition to the presence of neutral oxygen atoms, there are other neutral species, such as N_2, He, and O_2, with number densities at least ten times lower than the oxygen atoms, and there is also a small ionic component to the LEO atmosphere, of which the most abundant ion, O^+, is 10^4 times less dense than oxygen atoms.[2,4,5]

As spacecraft move in their orbits at relative velocities of about ~7.4 km s^{-1} (accounting for co-rotation of the orbit), they collide with the residual atmosphere.[6,7] At orbital altitudes of ~300-400 km, collisions between the spacecraft surfaces and ambient oxygen atoms have a mean collision energy around 108 kcal mol^{-1}. The roughly 1000 K kinetic temperature[1] of the atmosphere gives an energy spread (full width at half maximum) of ~48 kcal mol^{-1} to the collisions.[7] The collision energy of oxygen atoms striking exhaust plume species released from the spacecraft is not as well defined, as it is heavily dependent on the relative velocity between the two collision partners. The high-energy collisions between oxygen atoms and spacecraft surfaces lead to erosion and oxidation of surface materials, in particular polymers,

compromising the integrity of external surfaces,[8,9] while collisions between spacecraft exhaust species and oxygen atoms result in chemiluminescent products,[10] which have important implications in spacecraft tracking and surveillance, such as identification of the country of origin of a spacecraft or missile. Understanding the chemistry occurring during these high energy, or hyperthermal, collisions of oxygen atoms with spacecraft surfaces and with exhaust plume species is only beginning to be uncovered.

Polymer Erosion in LEO

Energetic collisions of oxygen atoms with spacecraft surfaces are considered to be one of the most important hazards to spacecraft in LEO, because such collisions can lead to eventual failure of exposed materials.[8,9] The detrimental effects of atomic oxygen in LEO were first recognized after post-flight analyses of polymer surfaces that were exposed during the earliest space shuttle flights.[11,12] The polymers showed a loss of surface gloss and concomitant weight loss. Concern over the degradation of materials by atomic oxygen sparked a huge effort, involving space- and ground-based studies, that has been aimed at the identification, understanding, and mitigation of problems caused by atomic oxygen in LEO.[13]

Despite such efforts, uncovering the details of the chemistry behind the oxygen atom erosion of polymers has been a formidable task. Progress towards understanding this chemistry has largely been accomplished, to varying degrees of success, by measuring mass loss during exposure of various polymers to oxygen atoms[14] and studying the chemical structure of the surface before, during, and after exposure.[15] While these approaches provide information about the net result of the complex reactions that are occurring at a polymer surface during exposure to atomic oxygen and allow inferences to be made about the chemical and physical interactions at the surface, they are an insensitive probe of the individual reaction and interaction mechanisms that combine to produce the net result. Experiments can be designed, however,

to study the individual steps of the overall erosion process, from initial interactions of oxygen atoms with a surface (initiation), to oxidation of carbon and scission of the hydrocarbon bond (propagation), and ultimate removal of volatile carbon-containing species (material loss).

Chemiluminescence From O-Atom Reactions with Rocket Plumes

Orbiting spacecraft in and missiles traveling through LEO exhaust plumes of combustion products and unburned fuel when using thrusters to adjust their position in orbit or to maintain their velocity. Other gaseous species, mostly H_2O, may be released from outgassing of materials in the space vacuum. Species within the exhaust plumes, which include fully and partially combusted fuel (including hydrocarbon fuel, in particular CH_4)[10], oxidizer, and possibly other chemical "countermeasures", interact with the ambient oxygen atoms at high center-of-mass (c.m.) collision energies forming internally excited products that produce radiative emissions around the space vehicle. Although some collisions have sufficient energy to form electronically excited products that can emit visible or ultraviolet radiation, it is more common for products to be formed with vibrational and rotational excitation, thus leading to emission of infrared radiation.[10] Both inelastic scattering, $O + X \rightarrow O + X^*$, and reactive scattering, $O + XY \rightarrow OX^* + Y^{**}$, can lead to infrared emissions.[10,16,17] Some efforts have been made to study these interactions in space by optical measurements of rocket firings or fuel dumps, but the experiments are costly and the spectra are extremely complicated by the complex environment.[10,18] More controlled studies can be made in the laboratory wherein identification of the chemical components released by a spacecraft from the spectral signatures can be accomplished by studying the products formed in the collisions and energy partitioning (i.e. electronic, translational, etc.) following the collisions. This information can then be used by theoreticians and modelers to calculate the expected emission spectra. Once the emission

spectra are known, the type of fuel used to propel the spacecraft or the gasses released around the vehicle can be determined. The ability to analyze and identify species in spectral signatures of spacecraft and missile plumes is considered to be a vital component of a modern missile defense.

From LEO to the Laboratory: Simulating Oxygen Atom Reactions Occurring in LEO

Recreating oxygen-atom reactions occurring in the LEO environment for controlled studies in the laboratory is no trivial task. In order to obtain the collision energy range observed in interactions occurring in LEO, experimentalists have two choices, one of which is accelerating a polymer or intact gaseous molecule, in a controlled fashion, to 7.4 km s^{-1} (16,500 mph), exposing it to a beam of thermal $O(^3P)$, and observing reactions occurring upon collision. The other is creating an oxygen atom beam with a velocity of 7.4 km s^{-1}, directing it to react with a stationary polymer surface or other slow-moving molecular collision partner, and making measurements during the collision. While neither option is simple, it is easier to create a high-velocity beam of atoms than accelerate a polymer or intact molecule to such high velocities. Creating a beam of oxygen atoms is an arduous endeavor because of their very high reactivity. Only a few sources of high-velocity oxygen atoms have been developed over the past 20 years. These include the ion neutralization, laser-sustained discharge, electron stimulated desorption, and laser detonation sources. A review of these and other lower energy oxygen atom sources may be found in Ref. 19. Of the sources mentioned, the laser detonation source has a relatively high flux and is well characterized in terms of beam velocity and by-products, such as light and ions. This source is also one of the only sources to be rigorously characterized in terms of the electronic states of the oxygen atoms in the beam; this work will be discussed in Chapter 3 of this thesis. Details on the operation of the laser detonation source are presented in Chapter 2.

Relevant Oxygen Atom Chemistry

Oxygen Atom Reactions with Hydrogen

While the $O(^3P) + H_2 \rightarrow OH + H$ reaction has only minor relevance to plume chemistry and hydrocarbon erosion in LEO, it is an important reaction for determining the electronic state composition of oxygen atoms produced from the laser detonation source without the use of spectroscopic methods, which are currently unavailable in our laboratory. The knowledge of the electronic state composition of the oxygen atom beam is a cornerstone upon which the understanding of all further reactions discussed in this thesis was built. While details of the beam characterization will be discussed in Chapter 3, a brief background on the $O(^3P)$, $O(^1D) + H_2$ reactions will be provided in this section.

Studies on the $O(^3P) + H_2 \rightarrow OH + H$ reaction span nearly 50 years largely because it is a prototype for hydrogen-atom abstraction reactions and is one of the key reactive steps in hydrogen and hydrocarbon combustion. The OH and H products are "simple" to detect experimentally and the reaction is amenable to thorough theoretical probing, offering a wealth of dynamical information, such as abstraction versus insertion mechanisms and curve crossing effects. Efforts to date have involved many theoretical and experimental approaches,[20-37] however, no experiments have been done that directly probe the reaction dynamics. The reason for this knowledge gap in this simple and prototypical triatomic system is partially due to the high reaction barrier, ~9 kcal mol^{-1}, and the small reduced mass of this system. Since the energy available for reaction is the center-of-mass collision energy, which is given by $E_{coll} = \frac{1}{2}\mu v_{rel}^2$, relative velocities near 8 km s^{-1} are required in order the achieve sufficient collision energy for the reaction to occur with thermal H_2. As discussed in the previous section, creating such an oxygen atom beam is an experimental challenge.

An additional experimental difficulty in studying the $O(^3P) + H_2$ reaction is the possible presence of the first electronic excited state of oxygen $O(^1D)$ in the oxygen atom reactant

beam. In contrast to the $O(^3P)$ reactions, the first electronic excited state of atomic oxygen, $O(^1D)$, which lies 45.4 kcal mol^{-1} higher in energy,[38] reacts readily with H_2 to form OH at very low collision energies, so small amounts of $O(^1D)$ in the oxygen atom beam would overshadow OH products from $O(^3P)$. The $O(^1D)$ reaction is exothermic (~41 kcal mol^{-1}) and barrierless,[39] and therefore the reaction cross sections are much larger than the analogous $O(^3P)$ reaction.[34,40] This stark difference in the reactivity of $O(^3P)$ and $O(^1D)$ is utilized in characterizing the electronic state composition of oxygen atoms produced from the laser detonation source discussed in Chapter 3.

Oxygen Atom Reactions with Alkanes

Much has been learned about $O(^3P)$ reactions with alkanes because of their relevance in combustion and atmospheric chemistry. Dynamical studies of oxygen atom reactions with various alkanes have shown that, at near thermal collision energies, an $O(^3P)$ atom typically reacts by abstracting a hydrogen atom to form an OH radical product, similar to the $O(^3P)$ + H_2 reaction.[41-43] Barriers for this reaction range from 5.0 to 8.1 kcal mol^{-1},[44] depending on the type of hydrogen abstracted (primary, secondary, or tertiary). These barriers are also reduced as the size of the hydrocarbon increases. Lower barriers coupled with larger reduced masses make these experiments more accessible to observe experimentally than the $O(^3P)$ + H_2 reaction. Several studies have been performed examining the kinetics and dynamics of hydrogen atom abstraction from various alkanes by $O(^3P)$, including theoretical calculation and experimental determination of reaction rates and vibrational and rotational distributions of the OH product.[41-47] A review of the hydrogen abstraction reaction by $O(^3P)$ from hydrocarbons was recently published by McKendrick *et al.*[45] All of these studies utilized fairly low collision energies conditions.

While it is well established that OH formation is the major channel in the reaction of alkanes with $O(^3P)$ at low collision energies, products, product energy, and angular distributions for reactions at collision energies representative of spacecraft-environment interactions have yet to be examined. It is easy to envision never before seen reaction channels when an oxygen atom reacts with alkanes at high c.m. collision energy, such as hydrogen atom elimination and possibly carbon-carbon bond breakage (in larger alkanes), if the collision energy is above the barriers for these processes. Prior to the work described in this thesis, only one limited theoretical study had considered the high collision energy regime present in LEO: Massa and coworkers performed *ab initio* calculations on the $O(^3P)$ reaction with ethane to form OCH_3 and CH_3 radicals.[48] They found a transition state structure and an activation barrier to the C-C bond breaking mechanism of about 41 kcal mol^{-1}. This channel was the only one considered in their calculations, although several more pathways are energetically possible.

Initial Reactions of $O(^3P)$ with a Hydrocarbon Surface

While it may seem counter intuitive to study reactions of gas-phase alkanes to elucidate mechanisms occurring on a surface, gas-phase-like processes have been observed in collisions of oxygen atoms with a saturated hydrocarbon surface.[19,49,50] In these experiments, which probe only the initial steps of the erosion process, 115 kcal mol^{-1} oxygen atoms were directed at a liquid hydrocarbon surface.[49,50] Only volatile reaction products could be detected in this experiment, and two products were observed: OH, which is formed via hydrogen atom abstraction by an oxygen atom, reminiscent of the gas-phase $O(^3P)$ + alkane reaction, and H_2O, formed from further reaction of the OH radical with the surface. In the formation of the OH product, the oxygen atom is believed to collide with a surface fragment of finite mass in

a localized interaction, similar to the interaction between an oxygen atom and a gas-phase hydrocarbon species. In fact, the effective mass of the surface fragment with which the oxygen atoms collided was found to be about 44 amu, the same mass as a propane molecule. This gas-phase-like formation of OH was determined to be one of the important first steps in the erosion process.

The observation that gas-phase-like reactions are occurring on surfaces led to using gas-phase hydrocarbons as collision partners for the oxygen atoms in order to study the dynamics, instead of the hydrocarbon surface. Reducing the size of the hydrocarbon reaction partner from a liquid, such as used in the experiment discussed above, squalane ($C_{30}H_{62}$), to a gaseous hydrocarbon, for example propane (C_3H_8), should lead to analogous results for the initial reactive events. However, since the alkanes are already in the gas phase, all reaction products formed, including possible oxygen-containing hydrocarbon species, would be detectable using the methods available and their dynamics could be examined. The smaller alkanes serve as excellent model systems to understand the reactions that can occur at surfaces and in spacecraft plumes. Furthermore, unlike the surfaces, these model systems can be treated in depth with modern theoretical methods. Chapters 5 and 6 in this thesis represent the first exploration into the reaction dynamics of hyperthermal atomic oxygen with saturated hydrocarbons by considering the reaction of $O(^3P)$ with the simplest hydrocarbon, methane.

Experiment-Theory Coupling

In the experiments undertaken, theoretical calculations done exclusively by Prof. George Schatz, Dr. Diego Troya, Dr. Biswajit Maiti, and Ronald Pascual at Northwestern University (NU) were invaluable in interpreting the data obtained. For every experiment, calculations were performed by Schatz at various levels of theory to serve not only as an invaluable aid to experimental data interpretation, but to refine codes developed at NU. The ultimate goal in

both of these efforts is to understand how a hydrocarbon polymer erodes in LEO and be able to model it reliably. None of the theoretical calculations herein are to be interpreted as the work of the author.

References

1. K. S. W. Champion, A. E Cole and A. J. Kantor, "Standard and Reference Atmospheres," *Handbook of Geophysics and the Space Environment*, Ed. A. S. Jursa (United States Air Force, Air Force Geophysics Laboratory, 1985).

2. R. G. Roble, "Energetics of the Mesosphere and Thermosphere," *The Upper Mesosphere and Lower Thermosphere: A Review of Experiment and Theory*, Eds. R. M. Johnson and T. L. Killeen (American Geophysical Union, Washington, D.C., 1995) pp. 1-21.

3. J. T. Visentine, "Environmental Definition of the Earth's Neutral Atmosphere," *NASA/ SDIO Space Environmental Effects on Materials Workshop held in Hampton, VA, 28 June - 1 July 1988*, NASA Conference Publication 3035, Part 1, Eds. L.A. Teichman and B.A. Stein (NASA, Washington, D.C., 1989) pp. 179-195.

4. *Natural Orbital Environmental Guidelines for Use in Aerospace Vehicle Development*, Eds. B. J. Anderson and R. E. Smith, NASA Technical Memorandum 4527 (NASA, Washington, D.C., 1994).

5. D. B. Green, G. E. Caledonia, and T. D. Wilkerson, *J. Spacecraft Rockets* **22**, 321 (1988).

6. E. Murad, *J. Spacecraft Rockets* **33**, 131 (1996).

7. B. A. Banks, K. K. deGroh, S. L. Rutledge and F. J. DeFilippo, *Prediction of In-Space Durability of Protected Polymers Based on Ground Laboratory Thermal Energy Atomic Oxygen*, NASA Technical Memorandum 107209 (NASA, Washington, D.C., 1996).

8. L. K. English, *Mat. Eng.* August, 39 (1987).

9. D. E. Hunton, *Sci. Am.* 261, 92 (1989).

10. F. S. Simmons, *Rocket Exhaust Plume Phenomenology* (American Institute of Aeronautics and Astronautics, Inc., Reston, VA, 2000).

11. L. J. Leger and J. T. Visentine, *J. Spacecraft Rockets* **23**, 505 (1986).

12. L. J. Leger, *Oxygen Atom Reaction with Shuttle Materials at Orbital Altitudes*, NASA Technical Memorandum 58246 (NASA, Houston, TX, 1982).

13. L. E. Murr and W. H. Kinard, *Am. Sci.* **81**, 153 (1993).

14. A. F. Whitaker and B. Z. Jang, *J. Appl. Polymer Sci.* **48**, 1341 (1993).

15. D. E. Brinza, S. Y. Chung, T. K. Minton, and R. H. Liang, *Final Report on the NASA/ JPL Evaluation of Oxygen Interactions with Materials-3 (EOIM-3)*, NASA JPL Publication (NASA, Pasadena, CA, 1994).

16. G. E. Caledonia, "Infrared Radiation Produced in Ambient/Spacecraft-Emitted Gas Interactions Under LEO Condition," in *Proceedings of the 38th AIAA Aerospace Sciences Meeting & Exhibit held in Reno, NV, 10-13 January, 2000*, AIAA-00-0104 (AIAA, Reston, VA, 2000).

17. B. L. Upschulte and G. E. Caledonia, *J. Chem. Phys.* **96**, 2025 (1992).

18. L. S. Berstein, Y-H. Chiu, J. A. Gardner, A. L. Broadfoot, M. I. Lester, M. Tsiouris, R. A. Dressler, and E. Murad, *J. Phys. Chem. A*, 107, 10695 (2003).

19. T. K. Minton and D. J. Garton, "Dynamics of Atomic-Oxygen-Induced Polymer Degradation in Low Earth Orbit," in *Advance Series in Physical Chemistry: Chemical Dynamics in Extreme Environments*, ed. R. Dressler (World Scientific, Singapore, 2000).

20. G. Dixon-Lewis and D. J. Williams, *Comp. Chem. Kinet.* **17**, 1 (1977).

21. N. Cohen and K. R. Westberg, *J. Phys. Chem. Ref. Data* **12**, 531 (1983).

22. N. Presser and R. J. Gordon, *J. Chem. Phys.* **82**, 1291 (1985).

23. S. Javoy, V. Naudet, S. Abid, and C. E. Paillard, *Int. J. Chem. Kinet.* **32**, 686 (2000).

24. G. C. Light, *J. Chem. Phys.* **68**, 2831 (1978).

25. J. Han, X. Chen, and B. R. Weiner, *Chem. Phys. Lett.* **332**, 243 (2000).

26. R. E. Howard, A. D. McLean, and W. A. Lester, *J. Chem. Phys.* **71**, 2412 (1979).

27. S. P. Walch, T. H. Dunning, R. Raffenetti, and F. W. Bobrowitz, *J. Chem. Phys.* **72**, 406 (1980).

28. J. S. Wright, D. J. Donaldson, and R. J. Williams, *J. Chem. Phys.* **81**, 397 (1984).

29. T. H. Dunning, Jr., L. B. Harding, A. F. Wagner, G. C. Schatz, and J. M. Bowman, *Science* **240**, 453 (1988).

30. T. Joseph, D. G. Truhlar, and B. C. Garrett, *J. Chem. Phys.* **88**, 6982 (1988).

31. S. Rogers, D. Wang, A. Kuppermann, and S. P. Walch, *J. Chem. Phys.* **104**, 2308 (2000).

32. B. R. Johnson and N. W. Winter, *J. Chem. Phys.* **66**, 4116 (1977).

33. R. Schinke and W. A. Lester, **70**, 4893 (1979).

34. G. C. Schatz, *J. Chem. Phys.* **83**, 5677 (1985).

35. D. C. Chatfield, R. S. Friedman, G. C. Lynch, D. G. Truhlar, and D. W. Schwenke, *J. Chem. Phys.* **98**, 342 (1993).

36. B. C. Garrett, D. G. Truhlar, and G. C. Schatz, *J. Am. Chem. Soc.* **108**, 2876 (1986).

37. A. F. Wagner and J. M. Bowman, *J. Chem. Phys.* **86**, 1976 (1987).

38. M. W. Chase, Jr., C. A. Davies, J. R. Downey, Jr., D. J. Frurip, R. A. McDonald, and A. N. Syverud, *J. Phys. Chem. Ref. Data* **14** (Suppl. 1), 531 (1639).

39. G. C. Schatz, L. A. Pederson, and P. J. Kuntz, *Faraday Discuss.* **108**, 357 (1997).

40. D. J. Garton, T. K. Minton, B. Maiti, D. Troya, and G. C. Schatz, *J. Chem. Phys.* **118**, 1585 (2003).

41. P. Andresen and A. C. Luntz, *J. Chem. Phys.* **72**, 5842 (1980).

42. N. J. Dutton, I. W. Fletcher, and J. C. Whitehead, *Mol. Phys.* **52**, 475 (1984).

43. G. M. Sweeney, A. Watson, and K. G. McKendrick, *J. Chem. Phys.* **106**, 9172 (1997).

44. J. T. Herron, *J. Phys. Chem. Ref. Data* **17**, 967 (1988).

45. F. Ausfelder and K. G. McKendrick, *Prog. React. Kinet. Mech.* **25**, 299 (2000).

46. M. C. Lin, "Dynamics of Oxygen Atom Reactions," in *Advances in Chemical Physics: Potential Energy Surfaces*, Ed. K. P. Lawley (John Wiley & Sons, Ltd., Chichester, Great Britain, 1980) pp. 113-167.

47. X. Liu and A. G. Suits, "The Dynamics of Hydrogen Atom Abstraction From Polyatomic Molecules," in *New Directions in Reaction Dynamics*, Eds. K. Liu and X. Yang (World Scientific, Singapore) to be published.

48. A. Gindulyte, L. Massa, B. A. Banks, and S. K. Rutledge, *J. Phys. Chem. A* **104**, 9976 (2000).

49. D. J. Garton, T. K. Minton, M. Alagia, N. Balucani, P. Casavecchia, and G. G. Volpi, *Faraday Discuss.* **108**, 387 (1997).

50. J. Zhang, D. J. Garton, and T. K. Minton, *J. Chem. Phys.* **117**, 6239 (2002).

METHODS

Crossed Molecular Beams Experiments

Crossed molecular beams methods provide a means to study fundamental gas-phase reaction dynamics under single-collision conditions. Y. T. Lee was a pioneer of "universal detection" in crossed-beams scattering experiments,[1-3] and he demonstrated the power of the crossed-beams method in elucidating the details of bimolecular collision dynamics. In his approach, two atomic or molecular beams are crossed at 90°, and products that scatter from the intersection region are detected with a mass spectrometer detector. The detector uses electron-impact ionization, which allows detection of a wide variety of products (thus the term "universal detection").

The hyperthermal oxygen atom reaction dynamics described in this thesis utilized a third generation crossed molecular beams apparatus based on the Y. T. Lee design.[1] A schematic diagram of the apparatus is shown in Fig. 2.1. A pulsed beam containing hyperthermal atomic oxygen is crossed at right angles by a pulsed supersonic beam of pure hydrogen or methane. Products that scatter from the intersection region are detected with a mass spectrometer detector (which rotates in the plane defined by the two beams) as a function of scattering angle and arrival time in the detector. Once ionized by the Brink-type electron-impact ionizer,[4] the products are mass selected with a quadrupole mass filter and counted with the use of a Daly-type ion counter.[5] The signal levels are always low enough that the detector is operated in a pulse counting mode, where electrical pulses resulting from individual ions emerge from the Daly ion counter and are accumulated as a function of their arrival time by a multichannel scaler. The ion flight time from the electron-impact ionizer to the Daly ion counter is proportional to the square root of the mass-to-charge ratio of the ion, and the

proportionality constant is determined empirically. Determination of the arrival time of neutral products at the electron-impact ionizer requires subtraction of the ion flight time from the time when ion counts are registered on the multichannel scaler. The number of ions generated in the electron-impact ionizer is dependent on the number density of neutral species present. Therefore, at a particular detector angle and mass-to-charge ratio, the mass spectrometer detector measures number density distributions as a function of arrival time, *N(t)*. These distributions are commonly referred to as time-of-flight (TOF) distributions. Integrated TOF distributions as a function of detector angle are called "laboratory angular distributions" and

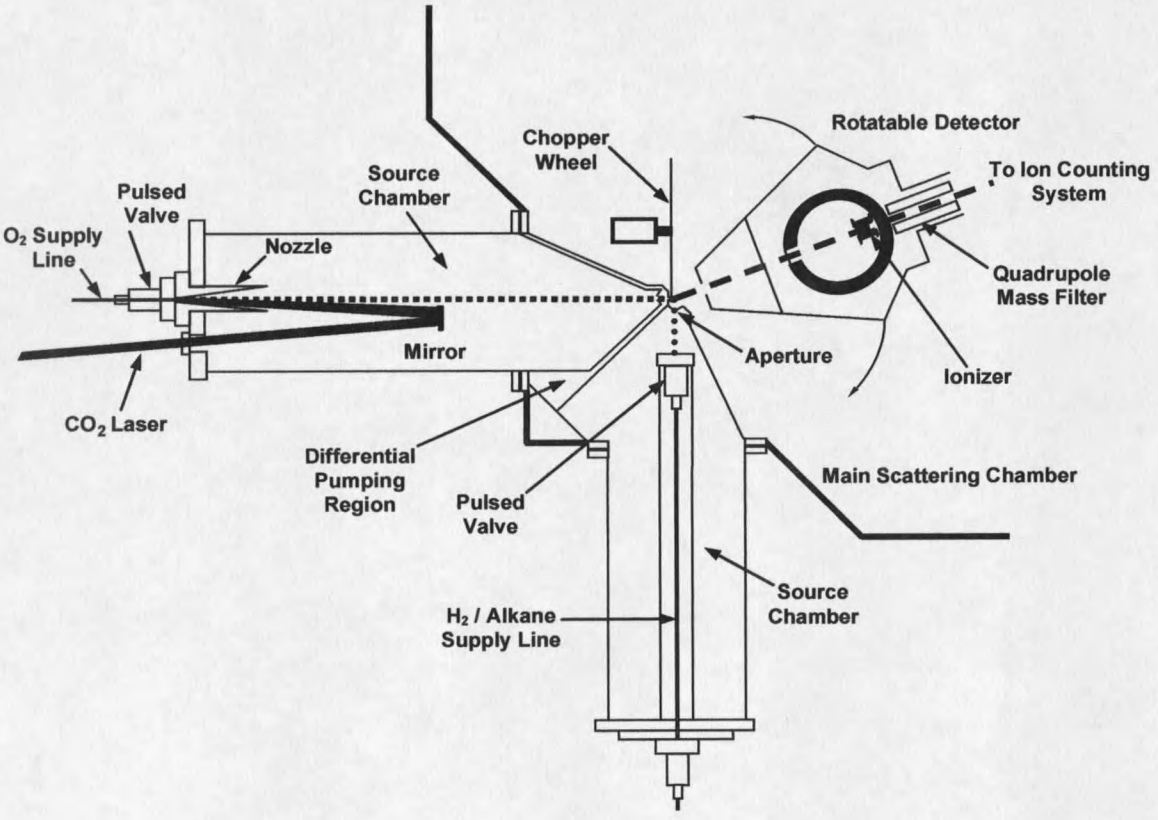

Figure 2.1. Schematic diagram of the crossed molecular beams apparatus at Montana State University. Components of the illustrated apparatus include the laser-detonation hyperthermal beam source, pulsed supersonic H_2/alkane source, differential pumping region, main scattering chamber, and rotatable mass spectrometer detector.

are given the designation $N(\Theta)$, where Θ is the angular direction of the scattered products with respect to the direction of the oxygen-atom beam. (The oxygen-atom beam direction is taken to be a laboratory angle of zero, and the positive angular direction is defined by a rotation from the oxygen-atom beam toward the hydrogen/alkane beam.) The primary data, then, are $N(t)$ and $N(\Theta)$ distributions of mass-selected products. In addition to detecting scattered products, the mass spectrometer detector is used to interrogate the atomic/molecular beams by aligning the detector such that the beam may enter it directly.

Beam Sources

Laser Detonation Source of Hyperthermal Atomic Oxygen

A unique and critical part of the research described herein is the laser detonation source (based on the source invented by Physical Sciences, Incorporated[6,7]), which provides a pulsed beam containing high velocity (6-9 km s^{-1}) oxygen atoms. The key elements of this source are a pulsed piezoelectric molecular beam valve,[8] a gold-plated, water-cooled copper nozzle, and a high energy (~7 J $pulse^{-1}$) CO_2 TEA laser. The pulsed valve introduces a high pressure (250 psig) surge (approximately 100 μs long) of pure O_2 gas into the conical nozzle through a 1 mm diameter × 250 mm long cylindrical channel at the apex of the cone. As the gas begins to expand into the nozzle, the CO_2 laser is fired, and the laser light passes through an antireflection-coated ZnSe window into the source chamber where it is then focused into the nozzle with the use of a bare gold mirror of 1 m radius of curvature. The beam waist of the laser is at the apex of the conical nozzle, but as the beam shape is roughly 4 × 4 mm at the waist, the laser light mainly impinges on the sides of the gold-coated cone and is reflected down into the orifice channel. The concentrated laser pulse initiates a breakdown of the gas and heats the resulting plasma to more than 20,000 K. The high-temperature, high-density

plasma expands rapidly into the 10 cm long, 20° included angle cone following detonation and engulfs the remaining cold gas. The local densities in the nozzle are sufficient to allow for efficient electron-ion recombination, but by the time the majority of the atoms formed in the plasma have cooled enough to recombine, the termolecular collision rate has dropped so low that the atomic species are, in effect, frozen in the emerging beam. Nevertheless, some atoms do recombine before the beam emerges from the nozzle, and the resulting beam thus contains both atomic and molecular oxygen. The ratio of atomic to molecular oxygen is variable depending on various source operating conditions, but the typical atomic fraction is about 70 percent. There is a small ionic component (<<1%), but any residual ions in the experiments described herein were deflected in a magnetic field produced by permanent magnets mounted on the source chamber roughly 50 cm downstream from the nozzle. The laser detonation source is generally operated at a repetition rate of 2 Hz, which is the practical limit allowed by the pumping speed of the source chamber. The pressure in the source chamber rises to ~1 mTorr during the gas pulse.

The hyperthermal beam is first collimated with the use of a 1 cm diameter aperture located 80 cm from the apex of the conical nozzle, and then the beam passes through a region of differential pumping (operating pressure ~10^{-6} Torr) and exits this region through a 3 mm diameter skimmer positioned ~95 cm from the apex of the nozzle. (In one experiment on the $O + D_2$ reaction, a smaller, 1.2 mm diameter, skimmer was used.) The hyperthermal beam reached the interaction region (the center of rotation of the detector) 99 cm from the nozzle apex, where it was only negligibly larger than the diameter of the previous skimmer. The operating pressure in the main scattering chamber was ~2×10^{-7} Torr.

The temporal profile of the atomic oxygen component of the overall hyperthermal beam pulse is seen in Fig. 2.2. The dashed line shows the TOF distribution of atomic oxygen, detected at $m/z = 16$. "Time zero" in this figure is the time at which the CO_2 laser fires, which